

ASCA Observation of the Crab-Like Supernova Remnant 3C58

Ken'ichi TORII,¹ Patrick O. SLANE,²

Kenzo KINUGASA,³ Kiyoshi HASHIMOTODANI,⁴ and Hiroshi TSUNEMI^{4,5,1}

¹ *NASDA TKSC SURP, 2-1-1 Sengen, Tsukuba, Ibaraki, 305-8505, Japan*

E-mail (KT) torii.kenichi@nasda.go.jp

² *Harvard-Smithsonian Center for Astrophysics, 60 Garden Street Cambridge, MA 02138, USA*

³ *Gunma Astronomical Observatory,*

6860-86 Nakayama, Takayama, Agatsuma, Gunma, 377-0702, Japan

⁴ *Department of Earth and Space Science, Graduate School of Science, Osaka University,*

1-1, Machikaneyama-cho, Toyonaka, Osaka, 560-0043, Japan

⁵ *CREST, Japan Science and Technology Corporation (JST)*

October 25, 2018

Abstract

We present here the X-ray observation of a Crab-like supernova remnant (SNR) 3C58 with ASCA. We find that the integrated energy spectrum over the nebula is consistent with previous results, showing a power-law spectrum with the photon index $\gamma = 2.2 - 2.4$ modified by interstellar absorption of about $(3 - 4) \times 10^{21} \text{ cm}^{-2}$. Inclusion of a blackbody component which is attributable to the central compact source significantly improves the spectral fit. Stringent upper limits for any line emitting thin hot plasma are established. We find for the first time that the nebular spectrum is harder in the central part of the SNR, becoming softer toward the periphery, while the absorption column is uniform across the nebula. Correspondingly, the nebular size decreases with increasing photon energy which is a steeper function of radius than that of the Crab nebula. The results are compared with

synchrotron energy loss models and the nature of the putative pulsar is discussed. Timing analysis was performed to search for pulsed X-ray emission from the central compact source. No significant pulsations are observed, and we present the upper limit for the pulsed fraction.

1 Introduction

The source 3C58 (G130.7+3.1) is believed to be the remnant of a historical supernova (SN) event in A.D. 1181 (e.g., Panagia, Weiler 1980). It shows a center-filled morphology both in the radio (e.g., Reynolds, Aller 1988) and X-ray bands (e.g., Becker et al. 1982). X-ray observations reveal a point-like source in the midst of the nebula (Becker et al. 1982) which contributes 7% of the total flux in the ROSAT HRI energy band (0.1-2.4 keV) (Helfand et al. 1995). The radio spectrum of the nebula is a power-law with an energy index of 0.1 (Green 1986) and the X-ray spectrum is a power-law with an energy index of 1.19 ± 0.12 (Asaoka, Koyama 1990). Though the central object itself is radio quiet, a wisp-like structure elongated in the north-south direction lies only 2.6 arcseconds west of the X-ray compact source (Frail, Moffett 1993). Similar wisp-like structures in the vicinity of the central objects are often found in the Crab-like SNRs, not only in the radio band (Bietenholz et al. 1991; Frail, Moffett 1993) but also in the optical band (Hester et al. 1995). These structures are believed to be associated with the termination of the relativistic pulsar wind by the ambient pressure. These characteristics, along with the nonthermal nature of the extended emission in 3C58, imply that the central source is a neutron star even though no coherent pulsations have been detected at any wavelength to date. From these characteristics, 3C58 is classified as a Crab-like SNR or a *plerion* (Weiler, Panagia 1978).

Though the Crab nebula and 3C58 have much in common, there are considerable differences as well. The radio and X-ray luminosities for 3C58 are factors of ~ 10 and ~ 2000 , respectively, below those of the Crab nebula (Helfand et al. 1995). As these objects are powered by the rotational energy loss of the central neutron star, the differences found in the surrounding nebulae should give insights into the properties of the young neutron stars.

The modeling of the Crab-like synchrotron nebulae has evolved with a strong bias on the Crab nebula itself due to its outstanding brightness. Models have been developed to explain the multi-wavelength spectrum and its evolution (e.g., Pacini, Salvati 1973; Reynolds, Chevalier 1984; Reynolds, Chanan 1984; Bandiera et al. 1996), the flow of relativistic particles and the corresponding morphology of the nebula (e.g., Rees, Gunn 1974; Aschenbach,

Brinkmann 1975; Kennel, Coroniti 1984a, b; Chiueh, Li, Begelman 1998). Following the model of Rees and Gunn (1974), Kennel and Coroniti (1984a, b hereafter KCa, b) proposed a magnetohydrodynamical (MHD) flow model with a standing shock having an extremely low magnetization parameter, σ (the ratio of the Poynting to particle energy fluxes in the upstream wind). This model successfully explains the previously observed variation in nebular size with energy from the optical to the hard X-ray band under the suitable boundary conditions.

The distance to 3C58 was derived by HI observations by several authors (Goss et al. 1973; Williams 1973; Green, Gull 1982; Roberts et al. 1993). Following the discussions made by Roberts et al. (1993), we adopt 3.2 kpc throughout this paper.

In this paper, we report the X-ray observation of 3C58 with the spectro-imaging detectors on board ASCA in the energy range 0.5–10 keV.

2 Observation and Data Reduction

3C58 was observed by ASCA (Tanaka et al. 1994) from 12 to 14 in September, 1995. As well as a proposed target of the AO3 observing phase, it was observed as an SIS (Solid-state Imaging Spectrometer) (Burke et al. 1994) calibration source. These observations were carried out with four different satellite attitudes. The fourth observation was made to obtain the accurate background in the adjacent region of the object. The SIS was operated in 1CCD mode with a read-out cycle of 4 s. The Gas Imaging Spectrometer (GIS), a position sensitive gas scintillation proportional counter (Ohashi et al. 1996; Makishima et al. 1996), was operated in PH mode. To search coherent pulsations, portions of the observation were carried out in a mode which allocates more bits to timing resolution than for standard observations. This sacrifices some spatial and spectral resolution. The time resolution of the GIS for the first observation was 1/16 s for high bit rate and 1/2 s for medium bit rate. For the other observations, the resolution was 1/1024 s and 1/128 s for high and medium bit rate, respectively. The observation date and the observation mode are summarized in table 1.

The raw data were screened with the standard screening parameters. The screening criteria restrict events to those obtained outside the South Atlantic Anomaly (SAA), for which the cut-off rigidity is > 6 GeV/c, and for which the angle of the source from the Earth rim is restricted to > 5 deg for the GIS, > 10 deg (25 deg) for the SIS for the dark (bright) Earth rim angle. For the SIS, flickering pixels are removed, only grades 0, 2, 3, and 4 are

selected, and four readout cycles are removed after the satellite passage of the SAA as well as after the satellite passage of the day-night transition. The effective exposure time after the data reduction is summarized in table 2 for each observation.

3 Results

3.1 Energy Spectrum of the Whole Remnant

We first investigated the energy spectrum of the whole SNR, including the compact source. To check the consistency between the detectors, energy spectra were extracted for each detector of each sensor using photons within 4 arcminutes from the emission center. The spectra were fitted with a power-law function modified by the interstellar absorption (Morrison, McCammon 1983). A formally acceptable fit was obtained for each data set by using this model. Since we found no significant systematic deviation above the level of the current status of the detector calibration of ASCA, we fitted the spectra from each observation simultaneously to improve the statistics. We show representative spectra in figure 1 and the best-fit spectral parameters are summarized in table 3.

Becker et al. (1992) obtained $\gamma = 1.5^{+0.5}_{-0.2}$ and $N_{\text{H}} = (1.8 \pm 0.5) \times 10^{21} \text{cm}^{-2}$ with the Einstein SSS, but a somewhat steeper power-law index ($\gamma = 2$) and approximately twice the column density using the IPC.

By fixing the absorption column to $N_{\text{H}} = 1.8 \times 10^{21} \text{cm}^{-2}$, the value determined with the Einstein SSS, Davelaar et al. (1986) obtained $\gamma = 2.30 \pm 0.26$ with the EXOSAT ME. Asaoka and Koyama (1990) obtained $\gamma = 2.19 \pm 0.12$ and $N_{\text{H}} < 10^{21.5} \text{cm}^{-2}$ with the Ginga LAC. Helfand et al. (1995) derived $\gamma = 1.70 \pm 0.30$ and $N_{\text{H}} = (3.25 \pm 0.7) \times 10^{21} \text{cm}^{-2}$ for the nebula by considering the Einstein SSS, IPC, ROSAT HRI, and the 21 cm (Green, Gull 1982) measurements, and a blackbody of 3.5×10^6 K for the central compact source. Taking into account the statistical and systematic errors of the data in the literature, these values are in reasonable agreement with those summarized in table 3. By using the first set of the SIS data, the observed flux is $1.3 \times 10^{-11} \text{ergs} \cdot \text{s}^{-1} \cdot \text{cm}^{-2}$ and the unabsorbed flux is $1.9 \times 10^{-11} \text{ergs} \cdot \text{s}^{-1} \cdot \text{cm}^{-2}$ in the range 0.5–10 keV. The statistical error in the flux determination is about 4% and the systematic error for the absolute flux is about 10%. The corresponding luminosity is $2.4 \times 10^{34} d_{3.2\text{kpc}}^2 \text{ergs} \cdot \text{s}^{-1}$ in the range 0.5–10 keV.

Though we see no line structure in the raw energy spectra by eye, we might expect some amount of thermal plasma of temperature $\sim 10^7 \text{K}$ that is shock-heated at the outgoing blast wave, and possibly at the reverse shock. To

search for evidence of such thermal emission, we performed the following analysis to establish limits on the emission measure ($EM = \int n_e n_H dV$, where n_e , n_H , and V denote the electron number density, the hydrogen number density, and the volume, respectively) by using a thin thermal plasma emission code.

We used the MEKAL model in XSPEC ver.9.0 which calculates the emission from an optically thin thermal plasma in collisional ionization equilibrium. The model includes line emission from heavy elements based on the model calculations of Mewe and Kaastra (e.g., Mewe et al. 1985) with the Fe L calculations by Liedahl et al. (1995). We assumed heavy elemental abundances equal to the solar values of Anders and Grevesse (1989). All the SIS and GIS data were used simultaneously to obtain the stringent upper limit. If both the power-law index and the absorption are allowed to vary, along with the thermal component, we find large absorption and a large power-law index which is incompatible with the Ginga result at higher energy (Asaoka, Koyama 1990). Therefore, we fix the power-law index and the absorption to be the best-fit values obtained without the thermal component. The resultant upper limit of the EM is shown in the upper panel of figure 2 for the assumed temperature range 0.1–12.8 keV. The corresponding upper limit of the rms density of the thermal plasma is shown in the lower panel assuming a spherical volume whose angular radius is 4 arcminutes. The solid line shows the limit when the filling factor is 1/4 which corresponds to the Sedov type self similar solution (Sedov 1993) and the dashed line shows the limit for a uniform sphere and the filling factor of unity.

Another possible thermal component is blackbody radiation from the cooling neutron star surface. A blackbody temperature of about 10^6 K from the entire surface, or an even higher temperature due to polar cap heating, may be expected (e.g., Yancopoulos et al. 1994; Slane 1994; Slane, Lloyd 1995; Helfand et al. 1995). Helfand et al. (1995) derived a crude constraint on the spectral shape of the compact source based on the flux ratio between the Einstein HRI and the ROSAT HRI. They obtained a blackbody temperature of 3.5×10^6 K and an emitting area of $\sim 4.5 \times 10^{10} d_{3.2\text{kpc}}^2 \text{ cm}^2$. To examine this component, we introduced a blackbody component to the simultaneous fit of all the SIS and GIS spectra. Without the blackbody component, the photon index, normalization of the power-law component, and the absorption column are $\gamma = 2.29 \pm 0.03$, $N = (4.8 \pm 0.2) \times 10^{-3} \text{ photons} \cdot \text{s}^{-1} \cdot \text{keV}^{-1} \cdot \text{cm}^{-2}$ at 1 keV, and $n_H = (4.0 \pm 0.2) \times 10^{21} \text{ cm}^{-2}$ with $\chi^2/\text{d.o.f.} = 1487/1330$. With the blackbody component, $\chi^2/\text{d.o.f.} = 1474/1328$ which shows that the blackbody component is significant at 99.7% level according to F-test. The best-fit spectral parameters are $T_{\text{blackbody}} = (5.1^{+0.6}_{-0.5}) \times 10^6 \text{ K}$ and the emitting area of $(1.2^{+0.8}_{-0.7}) \times 10^{10} d_{3.2\text{kpc}}^2 \text{ cm}^2$. The parameters for the power-law component and the absorption column are $\gamma = 2.1 \pm 0.1$, $N = (3.6 \pm 0.6) \times$

10^{-3} photons \cdot s $^{-1}$ \cdot keV $^{-1}$ \cdot cm $^{-2}$ at 1 keV, and $n_{\text{H}} = (3.3 \pm 0.4) \times 10^{21}$ cm $^{-2}$. With this model, the observed flux from the power-law and the blackbody component is 1.1×10^{-11} and 8.4×10^{-13} ergs \cdot s $^{-1}$ \cdot cm $^{-2}$ in the 0.5–10 keV range, respectively. The unabsorbed flux is 1.6×10^{-11} and 1.2×10^{-12} ergs \cdot s $^{-1}$ \cdot cm $^{-2}$, respectively. The corresponding luminosity is $L_{X,\text{pow}} = 2.0 \times 10^{34} d_{3.2\text{kpc}}^2$ ergs \cdot s $^{-1}$ and $L_{X,\text{blackbody}} = 1.5 \times 10^{33} d_{3.2\text{kpc}}^2$ ergs \cdot s $^{-1}$. We find the blackbody temperature derived here is ~ 1.5 times higher than that of Helfand et al. (1995) and the emitting area is ~ 3.8 times smaller. From the flux point of view, however, these two results are remarkably consistent within $\sim 20\%$. Thus we have confirmed the presence of a relatively high temperature blackbody component (Helfand et al. 1995) in the spectrum of the whole SNR. Due to the limited spatial resolution of ASCA and the limited spectral resolution of Einstein HRI and Rosat HRI, the temperature of the blackbody component can not be strictly constrained. The contribution from the blackbody component is further examined in the following spatially resolved analyses to confirm that it predominantly comes from the central compact source.

The power-law component of the X-ray spectrum determined with the power-law plus blackbody model is shown in figure 3 together with the radio (Green 1986; Salter et al. 1989 and the references therein), infrared (Green, Scheuer 1992; Green 1994), and γ -ray (Fichtel et al. 1994) data. The infrared and γ -ray data are the upper limits. The multi-wavelength spectrum of the Crab nebula is also shown in the figure for comparison (e.g., Saken et al. 1992; Wu 1981 and the references therein).

3.2 Energy Spectra of Concentric Annular Regions

The synchrotron lifetime of the electrons producing the X-ray emission varies as $\propto E^{-1}$. We thus expect a radial variation in the spectral index of the nebula with emission in the inner regions (where electron injection is most recent) exhibiting a flatter spectrum than for the outer regions. To investigate such a scenario, we performed spatially resolved spectral analysis. As the SIS has better spatial resolution than the GIS, we used only the SIS data for this analysis. We extracted energy spectra from concentric annular regions centered on the emission peak. The width of each annulus was 1 arcminute and the outer radii were 1, 2, 3, and 4 arcminutes. We first used a power-law function modified by the interstellar absorption to examine the systematic effect in the procedure and then introduced a blackbody component to the fit.

Since the point spread function (PSF) of ASCA X-ray telescope (XRT) (Serlemitsos et al. 1995) has a half power diameter of about 3 arcminutes, comparable in size with the 3C58 extended nebula, we conducted the analysis in the

following way to avoid the possible systematic effects. We first fitted the 3C58 data with all the model parameters free. We found that the power-law index was the flattest in the central region, steepening toward the periphery, while the absorption column was uniform across the nebula. To see the possible systematic effects, we applied the same procedure to the archival data of 3C273 (sequence number 71038020), a bright point source. We found neither the systematic steepening of the power-law index nor any systematic change of the absorption column depending on the radius. Since we found no significant systematic effects due to the instrumental response functions, we fitted the 3C58 data with the absorption column and the blackbody temperature (when included) fixed at the best-fit value obtained for the whole remnant to obtain statistically stringent limit on the other spectral parameters.

The resultant power-law indices are shown in figure 4 with 90% confidence errors. Squares show the result without the blackbody component and the circles show the result with the blackbody component. We find significant softening of the energy spectrum toward the periphery of the nebula, as expected from the synchrotron energy loss of the relativistic particles. Also, when the blackbody component is included, we find that the fraction of the flux from the blackbody component is about 10% in the inner part while it becomes negligibly weak at the outermost annulus (9.4%, 9.7%, 4.0%, and $< 0.6\%$ in the 0.5–10 keV range from the innermost toward the outermost annulus). This supports the interpretation that the blackbody radiation comes from the central source in 3C58. Thus we have shown that the spectrum consists of two components, one the spatially extended power-law component and the other a blackbody component at the center, and the former shows softening toward the periphery of the nebula. Since the spectral indices derived here are obtained after the convolution by the XRT PSF, we further quantify this softening in the following section in terms of the energy-size relation.

3.3 Image Fitting Analysis

In the method we adopted in the previous section, the spectrum for a given annulus is contaminated by the photons originating from the adjacent annuli due to the wings of the XRT PSF. In this section, we explore the spatial distribution of the energy spectrum using a different approach. We have extracted images in several energy ranges and fitted them with some appropriate function convolved by the PSF. In this method, the extracted image of each energy range does not suffer much from the photons whose energy is out of the energy range considered. This is justified for the SIS data due to its high energy resolution. We used subroutines and the standard calibration files provided by the instrumental team as part of the *jblidarf* and *ftools* packages to calculate the PSF. The azimuthal

structures due to the telescope quadrants are not taken into account in the PSFs in these functions.

Since we confirmed the blackbody component in the spectrum which is attributable to the compact source at the center of the nebula, we utilize a model function which comprises the nebula component, the compact source component, and the background component. We employ broad and narrow Gaussians for the compact source and the nebula, respectively. The model function is expressed as follows.

$$f(x, y) = A \cdot \exp\left(-\frac{(x - x_0)^2}{2\sigma_{1x}^2} - \frac{(y - y_0)^2}{2\sigma_{1y}^2}\right) + B \cdot \exp\left(-\frac{(x - x_0)^2}{2\sigma_{2x}^2} - \frac{(y - y_0)^2}{2\sigma_{2y}^2}\right) + C \quad (1)$$

where A , B , and C are the normalizations for the nebula, the compact source, and the background component, respectively; x and y are the positions in the right ascension and declination coordinate. Since the major axis of the nebular emission is well aligned in the east-west direction, we did not rotate the function around the center. The size of the nebula is characterized by σ_{1x} and σ_{1y} . σ_{2x} and σ_{2y} are fixed at 5 arcseconds which we find are appropriate to reproduce a compact source at the center. Since the contribution from the blackbody component to the observed flux is, based on the best fit spectral parameters, 7.9%, 15.6%, 16.7%, and 2.0% in the 0.5–1, 1–1.5, 1.5–3, and 3–10 keV range respectively, the ratio between A and B is fixed for each energy range to reproduce these fractions.

To examine the systematic error of the XRT PSF, we fitted the 3C58 images by using the 3C273 image as a PSF. A similar energy-size relation was obtained, but the derived sizes were different by +4%, +11%, +14%, and +11% in the EW direction and -6%, -8%, -11%, and -20% in the NS direction, in the 0.5–1, 1–1.5, 1.5–3, and 3–10 keV range, respectively. Thus we found at most 20% systematic error between the analyses made with the two kinds of PSFs. Since these systematic errors dominate the statistical errors, we quote 20% as the total error.

Figure 5 shows the azimuthally averaged radial profile of the data, the convolved model function, and the PSF. Figure 6 shows the position of the Gaussian center. Error bars show the 90% confidence positional uncertainty of ASCA which is 40 arcseconds (Gotthelf 1996; Gotthelf, Ishibashi 1997). We noted that the central position of the concentric annular regions used in the previous analyses agreed with the Gaussian centers within ~ 0.1 arcminutes. The absolute value of the Gaussian center is displaced about 40 arcseconds to the east compared with the position of the compact source determined by ROSAT HRI (Helfand et al. 1995), an offset which is consistent with the systematic positional uncertainty.

Figure 7 shows the size of the nebula as a function of the observing photon energy. The nebular size is found to show a monotonic decrease toward higher energy. A power-law fit for the nebular size as a function of the energy

yields

$$r_{\text{FWHM}}[\text{arcsec}] = (190 \pm 40) \times E[\text{keV}]^{-(0.5 \pm 0.2)} \quad (2)$$

in the east-west direction and

$$r_{\text{FWHM}}[\text{arcsec}] = (140 \pm 30) \times E[\text{keV}]^{-(0.5 \pm 0.2)} \quad (3)$$

in the north-south direction.

3.4 Timing Analysis

Though the emission characteristics of 3C58 strongly indicate the presence of a central pulsar, to date no coherent pulsations from the central object have been reported (Helfand et al. 1995). To search for a periodic signal from the central object, we performed a power spectral density (PSD) analysis on the GIS data. Photons extracted within 4 arcminutes from the emission center were used in the analysis. Barycentric corrections were made to the photon arrival times and a fast Fourier transformation (FFT) was applied to obtain the PSD. To improve the statistics, GIS2 and GIS3 data were co-added and they were analyzed by using a software developed by ourselves (e.g., Torii et al. 1997).

We found no significant pulsations at the 99% confidence level in the frequency range 0.01–64 Hz. The higher frequency range was limited by the time resolution of medium bit rate data. The upper limits for the pulsed fraction for a sinusoidal pulse shape were calculated according to the method described by Vaughan et al. (1994). The resultant 99% confidence upper limits for the entire selected region are summarized in table 4 for the three energy ranges, 0.7–10, 0.7–2, and 2–10 keV.

Since the number of photons is dominated by those originating from the nebula, with only $\sim 10\%$ originating from the central compact source, the pulsed fraction of the compact source is not tightly constrained. For the whole energy band (0.7–10 keV), the fraction of photons from the blackbody component expected from the best-fit spectral parameters is 11.7%. Therefore, if the blackbody component is pulsating, the upper limits for the pulsed fraction of the compact source are estimated as 62%, 82%, 80%, and 74% in the 0.01–1, 1–8, 8–32, and 32–64 Hz range, respectively.

4 Discussion

4.1 Multi-Wavelength Spectrum

Using the multi-wavelength spectrum of 3C58 shown in figure 3, we may investigate the time dependent energy loss properties of the nebula. In the following discussions we use the relation $F_X[\text{Jy}] = 10^{13.5} \cdot \nu[\text{Hz}]^{-1.1}$ derived from the best-fit spectral parameters of power-law plus blackbody model. This relation is shown by a dotted line in figure 3. For comparison between the Crab nebula and 3C58, we have summarized the basic parameters of these two objects in table 5.

As noted by Green and Scheuer (1992) (hereafter GS), a sharp break must exist around 5×10^{10} Hz by comparing the radio data with the infrared data, below which the relation $F_R[\text{Jy}] = 10^{2.3} \cdot \nu[\text{Hz}]^{-0.09}$ is applicable. Extrapolation of the X-ray spectrum back toward lower energies yields a flux density below the upper limits from IRAS data (Figure 3). However, standard synchrotron loss models for a power law distribution of electrons predict a radiated spectrum whose index beyond the break is 0.5 larger than the radio spectral index of ~ 0.1 . The fact that the X-ray energy index is much larger than 0.6 clearly rules out a single break under such a scenario.

Based on the energy loss model of Pacini and Salvati (1973), Bandiera et al. (1996) proposed that the low frequency spectral break for the plerionic component of the SNR G11.2-0.3 be identified with ν_c , a break associated with the radiative lifetime at τ , a characteristic slowing-down time scale of the pulsar, rather than ν_b , the break frequency associated with the radiative lifetime at the current time t (Pacini, Salvati 1973; Reynolds, Chanan 1984; Bandiera et al. 1996; Woltjer et al. 1997). If the break at $\nu \simeq 50$ GHz for 3C58 is due to the radiative lifetime at the current time, an unreasonably large magnetic field of $\gtrsim 3 \times 10^{-3}$ G has to exist in the nebula. We thus interpret this break as due to the decreasing energy output from the pulsar. However, a simple model does not reproduce the whole electromagnetic spectrum from radio through gamma-ray, and fine tuning of pulsar's braking law and the nebular expansion law seems to be needed (e.g., Reynolds, Chanan 1984). Further, if a second spectral break is invoked, it would still need to be at frequencies below $\sim 10^{12}$ Hz in order to be compatible with the IR upper limits. Woltjer et al. (1997) have shown that the sharpness of these breaks cannot be reproduced by any standard evolutionary scenario with a fixed braking index. Instead, their results support the suggestion by GS that a sudden reduction in the particle injection rate is required at some point in time.

Difficulties in reproducing the detailed spectra of plerionic remnants based on a single power-law particle distribution are well-known (Reynolds, Chevalier 1984; Reynolds, Chanan 1984; Atoyan, Aharonian 1996; Kennel,

Coroniti 1984a, b). In addition to an inherent change in the particle injection spectrum, there are other possible mechanisms which can lead to spectral breaks. In particular, the presence of multiple particle populations with different spectral properties can lead to such features. Such a scenario has some observational support. Fürst et al. (1988) observed the Crab-like SNR G21.5–0.9 at 22.3 GHz and compared the result with the Einstein HRI map previously obtained by Becker and Szymkowiak (1981); they noted that maximum X-ray emission coincides with a minimum in the radio emission. Recent *Chandra* observations of G21.5–0.9 (Slane et al. 2000) confirm the bright compact central X-ray emission, thus indicating a difference in the spatial distribution of at least some of the radio and X-ray producing particles. These results seem to suggest complex injection processes for radio and X-ray producing particles. However, we can not yet say whether this scenario holds for 3C58 with the currently available data.

4.2 Central Object

Observationally, a variety of X-ray spectra and pulse profiles have been reported for known rotation powered pulsars. Some show small duty cycle pulses with large pulsed fractions while others show sinusoidal pulse profiles with small pulsed fractions (e.g., Ögelman et al. 1993; Finley et al. 1992; Halpern, Ruderman 1993). Also, pulsed fractions are known to vary with photon energy.

If the X-ray spectrum of the pulsed component of the compact object in 3C58 is the same as that of the blackbody component determined from the spectral analysis, upper limits for the pulsed fraction of the compact source are obtained as 62–82% in the 0.7–10 keV band depending on the frequency range as described above. On the other hand, if the pulsed emission is hard, we may expect the number fraction of photons from the compact source to increase with increasing energy. From the simultaneous fit of all the SIS and GIS data using two power-law models modified by the interstellar absorption, of which one component has a photon index fixed at that for the Crab pulsar ($\gamma = 1.7$; Lyne, Graham-Smith 1990), we obtained an upper limit of 13% of the total counts for the number fraction from this component. Using this value, upper limits for the pulsed fraction for the compact source, in the case of the flat pulsar spectrum, are obtained as 56%, 74%, 72%, and 67% in the 0.01–1, 1–8, 8–32, and 32–64 Hz range, respectively, in the whole energy band (0.7–10 keV).

Helfand et al. (1995) obtained a blackbody temperature ($3.5 \times 10^6 \text{K}$) and an emitting area ($\sim 4.5 \times 10^{10} d_{3.2\text{kpc}}^2 \text{cm}^2$) for the central compact source. They found that the temperature is higher than that expected from any current

cooling models (e.g., Nomoto, Tsuruta 1987; Page, Applegate 1992) and that the associated emitting area is smaller than that expected from the whole neutron star surface. Therefore, they attributed the emission to a heated polar cap. We have confirmed the existence of a blackbody spectrum with the temperature of $T_{\text{blackbody}} = (5.1^{+0.6}_{-0.5}) \times 10^6$ K and the emitting area of $(1.2^{+0.8}_{-0.7}) \times 10^{10} d_{3.2\text{kpc}}^2 \text{ cm}^2$.

We can infer some of the properties of the neutron star by considering the empirical relationship between the X-ray luminosity, L_X , of pulsar/plerion systems and the spin-down power, \dot{E} , of the central pulsar derived by Seward and Wang (1988) based upon observations with the Einstein Observatory: $\log L_X = 1.39 \log \dot{E} - 16.6$. Adopting this relationship for 3C58, and converting the unabsorbed ASCA (0.5-10 keV) flux to the Einstein IPC bandpass (0.2-2.4 keV) for which the relationship was derived, we obtain $\dot{E} \sim 4 \times 10^{36} d_{3.2\text{kpc}}^2 \text{ ergs s}^{-1}$. This value of \dot{E} is two orders of magnitude smaller than that for the Crab pulsar, clearly indicating that not all young neutron stars are ‘‘Crab-like’’ in terms of their spin-down characteristics.

Assuming that the pulsar has spun down significantly from its initial period and has lost its rotational energy at the rate of the pure magnetic dipole radiation, the SNR age (814 yr assuming an association with SN 1181) and energy loss rate can be used to estimate the initial spin period (Seward and Wang 1988):

$$P = \left(\frac{2\pi^2 I}{\dot{E} t} \right)^{1/2} \approx 0.44 d_{3.2}^{-0.7} \text{ s}. \quad (4)$$

The spin-down rate is then $\dot{P} \sim 8.5 \times 10^{-12} d_{3.2}^{-1} \text{ s s}^{-1}$ and the surface magnetic field strength is $B \approx 6 \times 10^{13} d_{3.2}^{-0.7} \text{ G}$, which is at the high end of magnetic field values for the population of young pulsars. We note that variations as large as a factor of 10 or so are observed in the L_x vs. \dot{E} relationship, which could result in an overestimate of the field strength of more than a factor of 3. More importantly, relaxing the assumption that the initial spin period was much shorter than the current period leads to a broad range of permissible magnetic fields.

If the emitting area inferred from the blackbody component described above corresponds to a standard dipole-geometry polar cap, we may follow another path toward determining the spin properties of the central object (Helfand et al. 1995, equation (4); Lyne, Graham-Smith 1990, equation (14.7))

$$P = 58[\text{ms}] \left(\frac{r_{\text{cap}}}{0.6\text{km}} \right)^{-2} \left(\frac{R_*}{10\text{km}} \right)^3 \cos^2(90^\circ - \theta). \quad (5)$$

The notations are basically the same as those of Helfand et al. (1995); r_{cap} is the polar cap radius, R_* is the neutron

star radius, θ is the angle between the rotation and magnetic axes, and the units are in cgs unless otherwise specified. The spin down rate is thus $\dot{P} = 1.1 \times 10^{-12} [\text{s} \cdot \text{s}^{-1}] (\frac{r_{\text{cap}}}{0.6\text{km}})^{-2} (\frac{R_*}{10\text{km}})^3 \cos^2(90^\circ - \theta)$, and the current spin down power of the pulsar is $\dot{E} = 2.3 \times 10^{38} [\text{ergs} \cdot \text{s}^{-1}] (\frac{I_*}{10^{45}}) (\frac{r_{\text{cap}}}{0.6\text{km}})^4 (\frac{R_*}{10\text{km}})^{-6} \cos^{-4}(90^\circ - \theta)$.

The conversion rate of the spin down power to the power-law X-ray luminosity is

$$\frac{L_X}{\dot{E}} = 9 \times 10^{-5} (\frac{L_{X,\text{pow}}}{2.0 \times 10^{34}}) (\frac{I_*}{10^{45}})^{-1} (\frac{r_{\text{cap}}}{0.6\text{km}})^{-4} (\frac{R_*}{10\text{km}})^6 \cos^4(90^\circ - \theta) \quad (6)$$

which is anomalously low compared to other young objects (Seward, Wang 1988; Becker, Trümper 1997; Kawai, Tamura, Shibata 1998). This again leads to a relatively strong magnetic field ($\sim 10^{13}$ G), but we note that the \dot{E} result depends very strongly on the inferred polar cap size, which is quite uncertain. In particular, one of the uncertainties is the spectral fit by a simple blackbody model. More realistic models have been constructed and applied to several neutron star candidates (e.g., Zavlin, et al. 1996; Zavlin, et al. 1998). These models give a factor of $\simeq 2$ lower temperature and a factor of $\gtrsim 4$ larger emitting radius, values which are still too hot and too small to reconcile with emission from the entire surface of a neutron star. In the discussion below, we adopt the value of \dot{E} derived from the Seward & Wang (1988) relationship under the assumption that the spin-down power of the source in 3C58 is similar to that of other objects powering synchrotron nebulae.

4.3 Energy-Size Relation and the Particle Flow in the Nebula

The measured size of 3C58, and its dependence on energy, can be used to derive constraints on the particle flow in the nebula. The overall picture is as follows (see, e.g., KCa). A central pulsar injects energy into the nebula at a rate \dot{E} in the form of a relativistic particle wind. The wind zone is bounded by an MHD shock at a radius r_s beyond which the bulk particle flow is decelerated and the pressure is increased. A non-relativistic flow transports plasma and magnetic flux from the shock region to the edge of the nebula. Synchrotron emission from decelerated particles in a primarily toroidal magnetic field forms the observed nebula. Equipartition pressure of the magnetic field and the particle energy density drives the nebular expansion and determines the nebular structure. In this picture, an important parameter which characterizes the system is the magnetization parameter, σ , the ratio of the Poynting to particle energy fluxes in the upstream wind. The parameter can be constrained by applying pressure and flow boundary conditions at the edge of the nebula.

From radio observations (GS), the equipartition pressure in the nebula is estimated to be $P_{\text{neb}} \sim 10^{-10} \text{ dyn cm}^{-2}$,

which is also two orders of magnitude smaller than in the Crab nebula. The corresponding magnetic field of the nebula is $\sim 5 \times 10^{-5}$ G. Balancing the ram pressure of the wind, $\dot{E}/(4\pi cR_s^2)$, with the internal pressure of the nebula, we estimate that the distance from the pulsar to the confinement shock region is $R_s \sim 0.1$ pc. This corresponds to an angular size of ~ 6.5 arcsec. Using deep VLA imaging, Frail and Moffett (1993) discovered an elongated radio wisp just west of the compact X-ray source, which they argue is the termination shock from the pulsar wind. Using the ROSAT HRI position determination for the X-ray source (Helfand et al. 1995), the wisp lies at a distance of ~ 6.7 arcsec (0.1 pc) from the compact source, in excellent agreement with the above estimates. We note that Frail and Moffett (1993) quote an angular separation of 2.6 arcsec based upon the position determination of the compact source using Einstein HRI data; this difference is consistent with the ROSAT result considering the aspect determination errors of the two satellites. The radio wisp thus lies at a distance consistent with the estimated shock position and appears to represent a distinct signature of the termination shock.

From equation 5.15 of KCa, the magnetization parameter of the wind is related to the velocity profile of the nebula by $v(z) \approx 3\sigma[1 + (3\sigma z^2)^{-1/3}]$ where $z \equiv r/r_s$. The apparent size of the radio nebula ($10'.3 \times 6'.3$) yields a nebular size $r_N = (4.4 - 2.9)d_{3.2}$ pc. It is interesting to note that this yields $r_N/r_s \approx 15 - 100$ which is similar to that for the Crab (~ 20). Using the age of 814 yr thus gives a mean expansion velocity of $(5.4 - 3.5) \times 10^8 d_{3.2}$ cm s $^{-1}$. Assuming homologous expansion, the current velocity is 2/5 of the averaged value. Thus, using $z_N = r_N/r_s$ we find $\sigma \sim (2 - 6) \times 10^{-3}$, comparable to that for the Crab nebula. Alternatively, constant velocity of expansion leads to $\sigma \sim (6 - 15) \times 10^{-3}$. Thus, the prime assumption of the KC model, namely a small magnetization parameter corresponding to a particle-dominated wind, is valid here.

Well beyond the wind termination shock, the magnetic field in the nebula is primarily the wound-up field from the pulsar. The radial profile of this toroidal field is $B(r) \propto [rv(r)]^{-1}$ (Aschenbach, Brinkmann 1975; Ku et al. 1976). Under the assumption of a power law velocity profile $v(r) \propto r^{-m}$ (Aschenbach, Brinkmann 1975), the magnetic field strength then varies as $B(r) \propto r^{m-1}$. Due to the finite synchrotron lifetime of the emitting electrons, the measured nebular radius is a function of the observed photon energy: $r \propto E^{-1/(6m-2)}$ (Aschenbach and Brinkmann 1975). Using the measured energy dependence of the nebular size summarized in Section 3.3, we find $m = 0.7_{-0.1}^{+0.2}$ for both EW and NS directions. The magnetic field strength thus decreases slowly with radius. For the Crab nebula, Ku et al. (1976) find an energy-size relationship which leads to $m = 1.46_{-0.08}^{+0.10}$. The velocity law is thus flatter for 3C58, indicating a smaller deceleration of the particle flow in the nebula which corresponds with the smaller inferred

confinement pressure for 3C58 relative to that for the Crab.

From the above discussion, we propose a semi-quantitative picture of 3C58 as follows. The current spin-down power of the central pulsar in 3C58 is $\dot{E} \sim 4 \times 10^{36}$ erg s⁻¹ which is two orders of magnitude smaller than that of the Crab pulsar. From radio observations, the equipartition pressure in the nebula is $\sim 10^{-10}$ dyn cm⁻² which is also about two orders of magnitude smaller than for the Crab nebula. Consequently, the position of the standing shock where the ram pressure of the pulsar wind balances the nebular pressure is at about the same distance from the pulsar, $r_s \sim 0.1$ pc, for both 3C58 and the Crab. The magnetization parameter $\sigma \sim (2 - 15) \times 10^{-3}$ is of roughly the same order as that for the Crab, indicating a particle-dominated flow at the point of injection. Using these parameters, we obtain the upstream magnetic field (KCb, equation 2.2) as $B_1 = 2.6 \times 10^{-6} (\dot{E}/(4 \times 10^{36} \text{ erg s}^{-1}))^{1/2} (\sigma/(5 \times 10^{-3}))^{1/2} (r_s/0.1 \text{ pc})^{-1}$ G. The downstream magnetic field is amplified by a factor of 3 for the small σ limit (KCc, equation 4.15d) and $B_2 \sim 7.8 \times 10^{-6}$ G. The magnetic field in the inner regions increases with increasing radius, and reaches the equipartition value of $\sim 5 \times 10^{-5}$ G at a radius $\bar{r} = r_s \bar{z} = r_s (3\sigma)^{-1/2} \sim 0.8$ pc. If we approximate the bulk motion velocity in the nebula by a power law, we find a flatter profile than for the Crab, indicating a slowly decreasing magnetic field strength in the outer nebula and a smaller deceleration with lower confinement pressure in 3C58 than for the Crab.

5 Conclusion

With the broad band spectroscopic capability of ASCA, we have obtained accurate X-ray spectra of the SNR 3C58. Using both the SIS and GIS spectra, we find the integrated emission to be best described by a power law with $\gamma = 2.1 \pm 0.1$ accompanied by a blackbody with $T_{\text{blackbody}} = (5.1_{-0.5}^{+0.6}) \times 10^6$ K and an emitting area of $(1.2_{-0.7}^{+0.8}) \times 10^{10} d_{3.2}^2$ cm². The column density is $N_H = (3.3 \pm 0.4) \times 10^{21}$ cm⁻². We associate the blackbody component with the central compact X-ray source in the remnant. No pulsations are detected from the central emission in 3C58. We set upper limits of $\sim 55 - 80\%$ for the pulsed fraction of the compact source, depending upon the spectral characteristics of any pulsed emission.

Using images of the nebula in different energy bands, we have established the spectral softening with radius expected for a synchrotron spectrum injected from a central source. We have used these results to obtain, for the first time, the energy-size relation for the 3C58 nebula. By comparing this result to model of Aschenbach and

Brinkmann (1975) we find the bulk motion velocity and the magnetic field strength to be flatter functions of radius than for the Crab nebula. In addition, we have used the results to derive constraints on the interior pressure and magnetic field, as well on the shock magnetization parameter, using the models of KC. Small confinement pressure and the small deceleration of expansion of the 3C58 nebula has been suggested for the 3C58 nebula compared to the Crab.

The authors are grateful to the referee, Dr. Robert Petre, for invaluable comments and suggestions, which largely improved the draft. The authors are grateful to all the members of the ASCA team. KT was supported in part by Research Fellowships of the Japan Society for the Promotion of Science for Young Scientists. POS is supported in part by NASA Contract NAS8-39073 and Grants NAG5-2638 and NAG5-3486.

References

- Anders E., Grevesse N. 1989, *Geochimica et Cosmochimica Acta* 53, 197
- Asaoka I., Koyama K. 1990, *PASJ* 42, 625
- Aschenbach B., Brinkmann W. 1975, *A&A* 41, 147
- Atoyán A.M., Aharonian F.A. 1996, *MNRAS* 278, 525
- Bandiera R., Pacini F., Salvati M. 1996, *ApJL* 465, L39
- Becker R.H., Szymkowiak A.E. 1981, *ApJL* 248, L23
- Becker R.H., Helfand D.J., Szymkowiak A.E. 1982, *ApJ* 255, 557
- Becker W., Trddotumper J. 1997, *A&A* 326, 682
- Bietenholz M.F., Frail D.A., Hankins T.H. 1991, *ApJL* 376, L41
- Burke B.E., Mountain R.W., Daniels P.J., Cooper M.J., Dolat V.S. 1994, *IEEE Trans. Nuclear Science* 41, 375
- Chiueh T., Li Z.-Y., Begelman M.C. 1998, *ApJ* 505, 835
- Davelaar J., Smith A., Becker R.H. 1986, *ApJL* 300, L59
- Fichtel C.E., Bertsch D.L., Chiang J., Dingus B.L., Esposito J.A., Fierro J.M., Hartman R.C., Hunter S.D. et al. 1994, *ApJS* 94, 551
- Finley J.P., Ögelman H., Kiziloglu U. 1992, *ApJL* 394, L21
- Frail D.A., Moffett D.A. 1993, *ApJ* 408, 637
- Fürst E., Handa T. Morita K., Reich P., Reich W., Sofue Y. 1988, *PASJ* 40, 347
- Goss W.M., Schwartz U.J., Wesselius P.R. 1973, *A&A* 28, 305
- Gotthelf E. 1996, *ASCA News* 4, p31
- Gotthelf E., Ishibashi K. 1997, *X-ray Imaging and Spectroscopy of Cosmic Hot Plasmas*, ed Makino F., Mitsuda K. (Universal Academy Press, Tokyo) p631
- Green D.A., Gull S.F. 1982, *Nature* 299, 606
- Green D.A. 1986, *MNRAS* 218, 533
- Green D.A., Scheuer P.A.G. 1992, *MNRAS* 258, 833 (GS)
- Green D.A. 1994, *ApJS* 90, 817
- Halpern J.P., Ruderman M. 1993, *ApJ* 415, 286
- Helfand D.J., Chanan G.A., Novick R. 1980, *Nature* 283, 24
- Helfand D.J., Becker R.H., White R.L. 1995, *ApJ* 453, 741
- Hester J.J., Scowen P.A., Sankrit R., Burrows C.J., Gallagher III J.S., Holtzman J.A., Watson A., Trauger J.T. et al. 1995, *ApJ* 448, 240
- Kawai, N., Tamura, K., Shibata, S. 1998, *Neutron Stars and Pulsars Thirty Years after the Discovery*, ed. N. Shibasaki, N. Kawai, S. Shibata, & T. Kifune (Tokyo: Universal Academy Press), 449
- Kennel C.F., Coroniti F.V. 1984, *ApJ* 283, 694 (KCa)
- Kennel C.F., Coroniti F.V. 1984, *ApJ* 283, 710 (KCb)
- Ku W., Kestenbaum H.L., Novick R., Wolf R.S. 1976, *ApJL* 204, L77
- Liedahl D.A., Osterheld A.L., Goldstein W.H. 1995, *ApJL* 438, L115
- Lyne A.G., Graham-Smith F. 1990, *Pulsar Astronomy* (Cambridge University Press, Cambridge)
- Makishima K., Tashiro M., Ebisawa K., Ezawa H., Fukazawa Y., Gunji S., Hirayama M., Idesawa E. et al. 1996, *PASJ* 48, 171
- Mewe R., Gronenschild E.H.B.M., van den Oord G.H.J. 1985, *A&AS* 62, 197
- Morrison R., McCammon D. 1983, *ApJ* 270, 119
- Nomoto K., Tsuruta S. 1987, *ApJ* 312, 711
- Ohashi T., Ebisawa K., Fukazawa Y., Hiyoshi K., Horii M., Ikebe Y., Ikeda H., Inoue H. et al. 1996, *PASJ* 48, 157
- Ögelman H., Finley J.P., Zimmerman H.U. 1993, *Nature* 361, 136
- Pacini F., Salvati M. 1973, *ApJ* 186, 249
- Page D., Applegate J.H. 1992, *ApJL* 394, L17
- Panagia N., Weiler K.W. 1980, *A&A* 82, 389
- Rees M.J., Gunn J.E. 1974, *MNRAS* 167, 1
- Reynolds S.P., Chevalier R.A. 1984, *ApJ* 278, 630
- Reynolds S.P., Chanan G.A. 1984, *ApJ* 281, 673
- Reynolds S.P., Aller H.D. 1985, *AJ* 90, 2312
- Reynolds S.P., Aller H.D. 1988, *ApJ* 327, 845
- Roberts D.A., Goss W.M., Kalberla P.M.W., Herbstmeier U., Schwarz U.J. 1993, *A&A* 274, 427
- Saken J.M., Fesen R.A., Shull J.M. 1992, *ApJS* 81, 715
- Salter C.J., Reynolds S.P., Hogg D.E., Payne J.M., Rhodes P.J. 1989, *ApJ* 338, 171
- Sedov L.I. 1993, *Similarity and dimensional methods in mechanics 10th edition* (CRC Press, Boca Raton)
- Serlemitsos P.J., Jalota L., Soong Y., Kunieda H., Tawara Y., Tsusaka Y., Suzuki H., Sakima Y. et al. 1995, *PASJ* 47, 105
- Seward F.D., Harnden F.R., Helfand D.J. 1984, *ApJL* 287, L19

Seward F.D., Wang Z.R. 1988, ApJ 332, 199
Slane P. 1994, ApJ 437, 458
Slane P., Lloyd N. 1995, ApJL 452, L115
Slane P., Chen Y., Schulz N.S., Seward F.D., Hughes J.P., Gaensler B.M. 2000, ApJL in press
Tanaka Y., Inoue H., Holt S.S. 1994, PASJ 46, L37
Toor A., Seward F.D. 1974, AJ 79, 995
Torii K., Tsunemi H., Dotani T., Mitsuda K. 1997, ApJL 489, L145
Vasisht G., Aoki T., Dotani T., Kulkarni S.R., Nagase F. 1996, ApJL 456, L59
Vaughan B.A., van der Klis M., Wood K.S., Norris J.P., Hertz P., Michelson P.F., van Paradijs J., Lewin W.H.G. et al. 1994, ApJ 435, 362
Weiler K.W., Panagia N. 1978, A&A 70, 419
Williams D.R.W. 1973, A&A 28, 309
Woltjer L., Salvati M., Pacini F., Bandiera R. 1997, A&A 325, 295
Wu C-C. 1981, ApJ 245, 581
Yancopoulos S., Hamilton T.T., Helfand D.J. 1994, ApJ 429, 832
Zavlin V.E., Pavlov G.G., Shibanov Yu.A. 1996, A&A 315, 141
Zavlin V.E., Pavlov G.G., Trümper J. 1998, A&A 331, 821

Figure captions

Figure 1: Representative energy spectra of the whole SNR obtained by S0C1 and GIS2. The solid lines in the spectra show the best fit power-law model modified by the interstellar absorption. The lower panels show the residuals.

Figure 2: Upper panel shows the upper limits of the emission measure of the thermal component of MEKAL model. Lower panel shows the upper limits of the density for the filling factor of unity (dashed line), and the filling factor of 1/4 (solid line) which corresponds to the Sedov type self similar solution.

Figure 3: Multi-wavelength spectra of the Crab nebula (dashed line) and 3C58. The dotted line shows the extrapolation of the X-ray spectrum.

Figure 4: Photon index of the power-law component as a function of radius with 90% confidence errors. Squares show the case without the blackbody component and the circles show the case with the blackbody component.

Figure 5: Radial profile of the image, the best-fit model function and the PSF as the results of the fitting. Crosses show the data points, circles show the best-fit model function and the triangles show the PSF.

Figure 6: Position of the Gaussian center, x_0 and y_0 in equatorial coordinate (Epoch 2000).

Figure 7: The size of the nebula as a function of the observing energy.

Table 1: Observation date and mode.

Number	Start Time (UT)	End Time (UT)	SIS0	SIS1	GIS2	GIS3
1	14:13 Sep. 12, 1995	07:50 Sep. 13, 1995	C1	C3	PH nominal	PH nominal
2	07:05 Sep. 13, 1995	17:20 Sep. 13, 1995	C0	C2	PH timing	PH timing
3	17:21 Sep. 13, 1995	04:00 Sep. 14, 1995	C2	C0	PH timing	PH timing
4	04:01 Sep. 14, 1995	14:00 Sep. 14, 1995	C1	C3	PH timing	PH timing

Table 2: Effective exposure time [ks].

Number	SIS0	SIS1	GIS2	GIS3
1	22.05	22.19	27.14	27.05
2	12.31	12.31	15.28	15.37
3	15.24	15.34	18.08	18.08
4	13.91	13.93	16.98	16.96

Table 3: Spectral parameters of the whole nebula with the 90% confidence errors. Photon index (γ), normalization ([photons \cdot s $^{-1}$ \cdot keV $^{-1}$ \cdot cm $^{-2}$] at 1 keV), and the absorbing column density (n_{H} [10 21 cm $^{-2}$]) are summarized.

	S0C1 + S1C3	S0C0 + S1C2	S0C2 + S1C0	G2 + G3
γ	2.24 ± 0.05	2.21 ± 0.08	$2.26^{+0.07}_{-0.06}$	2.32 ± 0.07
Normalization	$(4.9^{+0.3}_{-0.2}) \times 10^{-3}$	$(4.6 \pm 0.4) \times 10^{-3}$	$(4.7 \pm 0.3) \times 10^{-3}$	$(4.7 \pm 0.4) \times 10^{-3}$
n_{H}	3.7 ± 0.2	4.0 ± 0.4	4.1 ± 0.3	3.5 ± 0.5
$\chi^2/\text{d.o.f.}$	302.1/337	289.2/280	354.1/315	436.3/396

Table 4: 99% confidence upper limits of pulsed fraction in %.

Frequency Range [Hz]	Energy Range [keV]		
	0.7–10	0.7–2	2–10
0.01–1	7	12	11
1–8	10	14	9
8–32	9	19	15
32–64	9	14	12

Table 5: Basic parameters of the Crab nebula and 3C58.

	Crab	3C58
Distance [kpc]	2	3.2
Age [yr] in 1995	941	814
Size [pc] ^a	1.2	2.9×2.2
L_X [ergs s $^{-1}$] ^b	2.1×10^{37}	2.4×10^{34}
ν_B [Hz] ^c	1×10^{13}	5×10^{10}

Notes. — ^a The size of the nebula at 1 keV defined by the Gaussian FWHM. The value for the Crab nebula is based on Ku et al. (1976).

^b Total (nebula plus compact source) X-ray luminosity in the energy range 0.5–10 keV. The value for the Crab nebula is based on Toor and Seward (1974).

^c Frequency of the spectral break. The values are adopted from Green (1994) and the references therein.

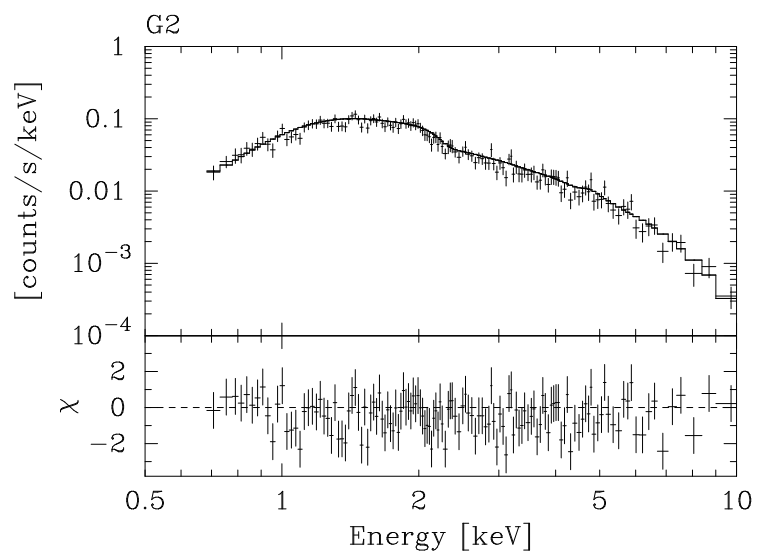
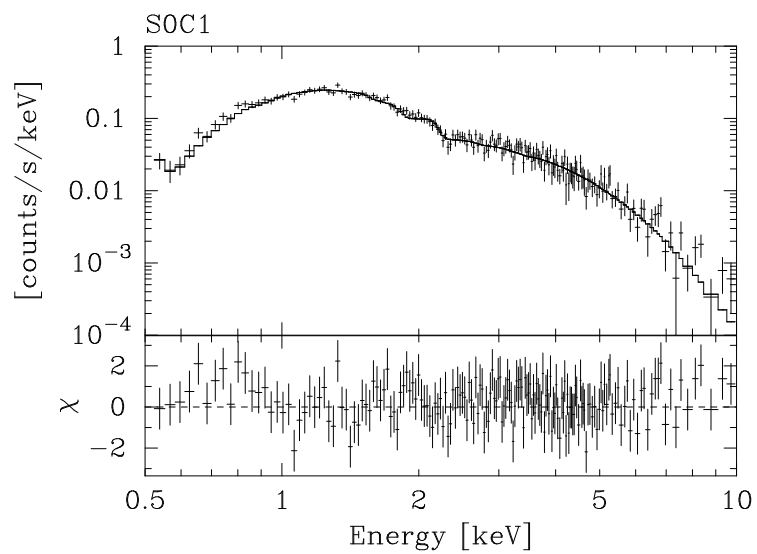


Figure 1:

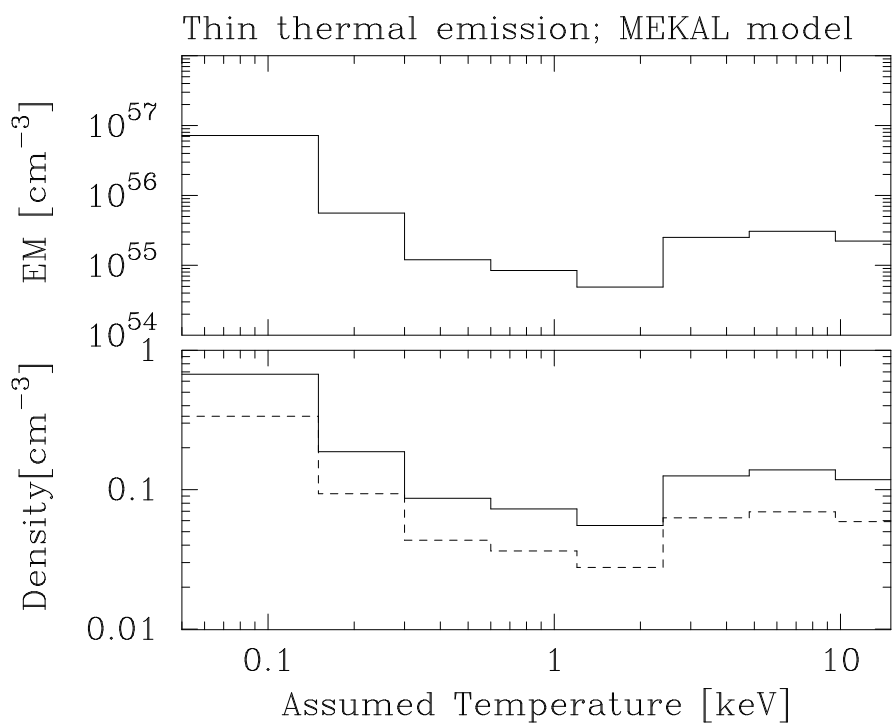


Figure 2:

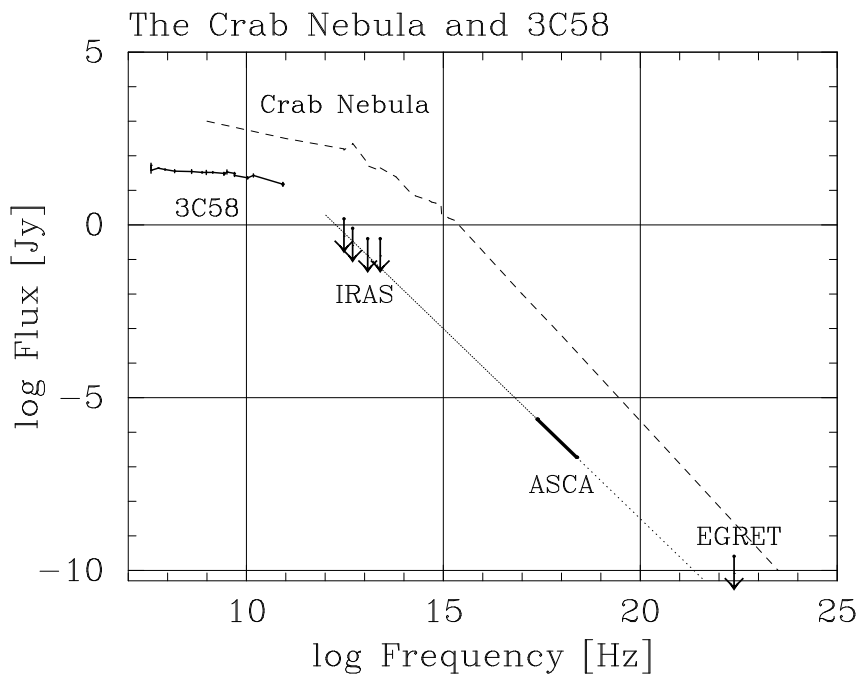


Figure 3:

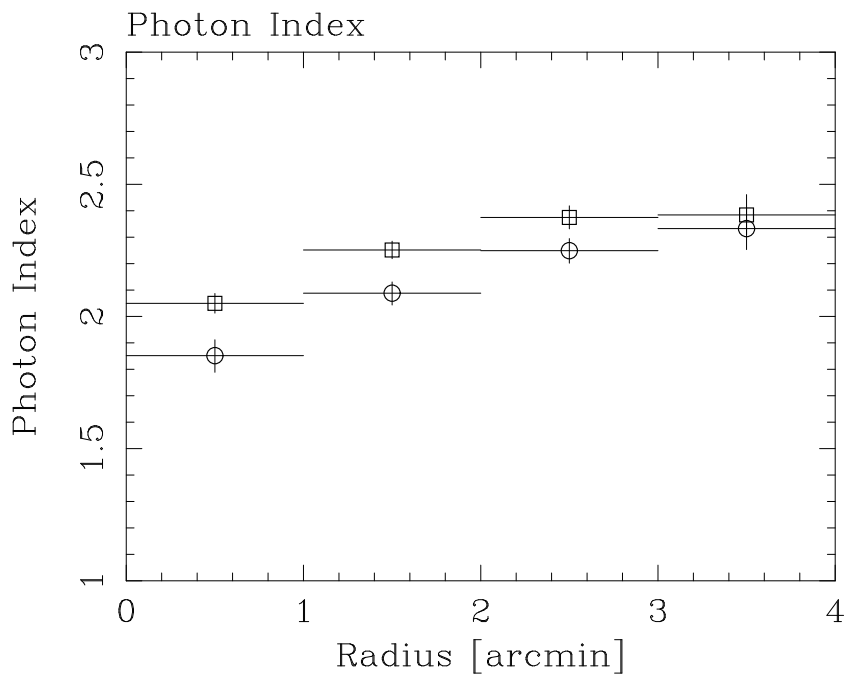


Figure 4:

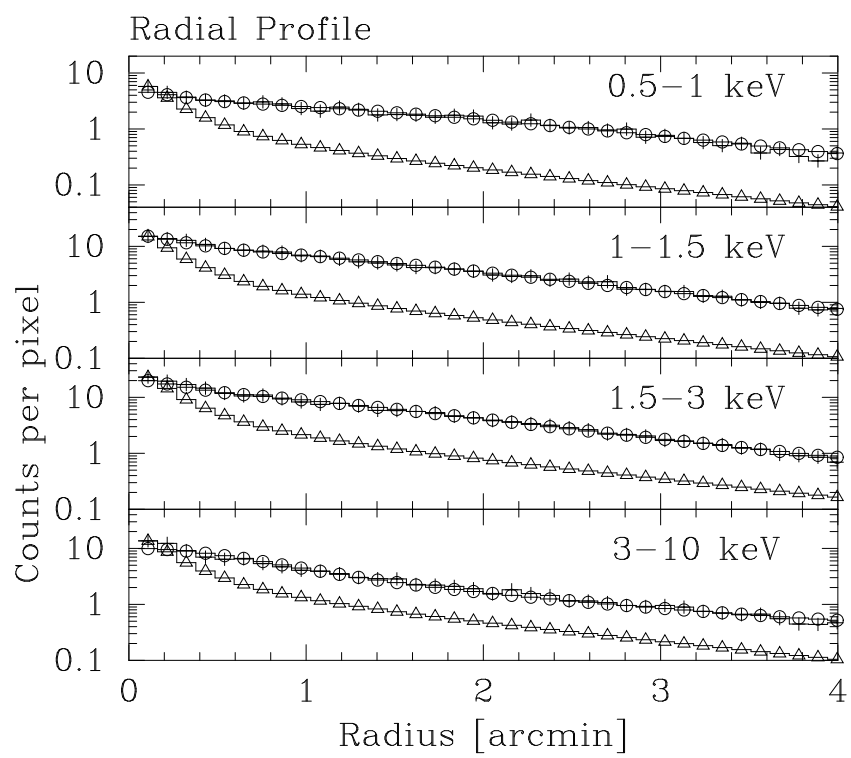


Figure 5:

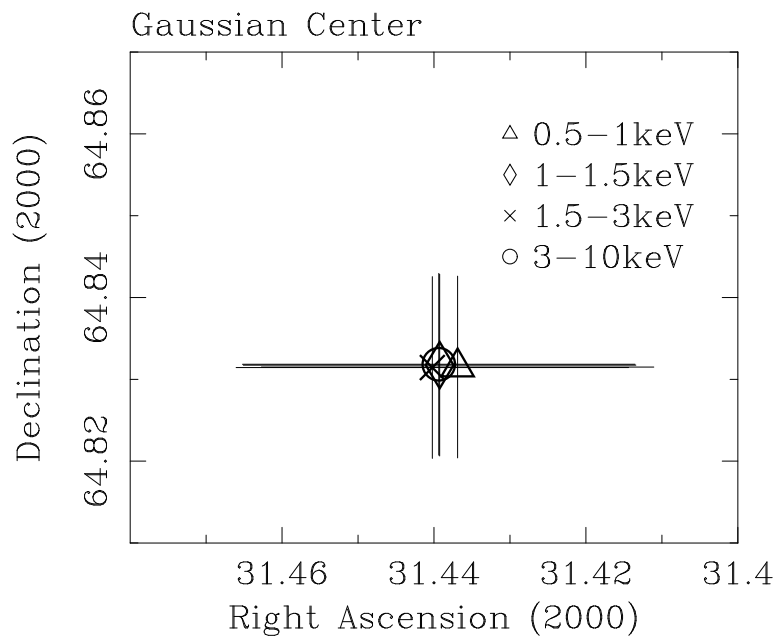


Figure 6:

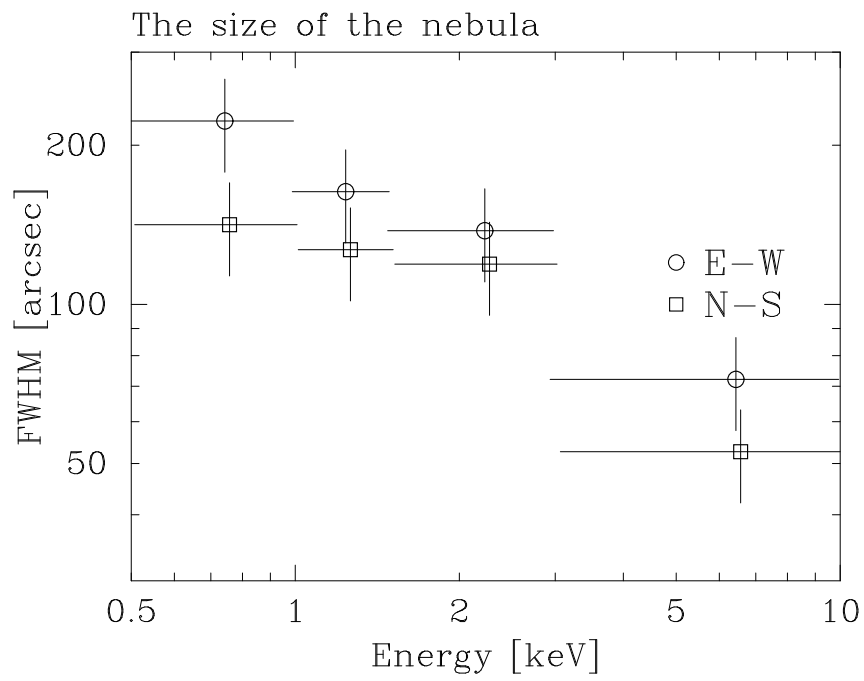


Figure 7: